

Soft X-ray Transmission Spectroscopy of Warm/Hot Intergalactic Medium with XEUS

Hajime KAWAHARA¹, Kohji YOSHIKAWA¹, Shin SASAKI², Yasushi SUTO¹,
Nobuyuki KAWAI³, Kazuhisa MITSUDA⁴, Takaya OHASHI², and Noriko Y. YAMASAKI⁴

¹*Department of Physics, School of Science, The University of Tokyo, Tokyo 113-0033*
kawahara@utap.phys.s.u-tokyo.ac.jp

²*Department of Physics, Tokyo Metropolitan University,*
1-1 Minami-Osawa, Hachioji, Tokyo 192-0397

³*Department of Physics, Tokyo Institute of Technology,*
2-12-1 Ookayama, Meguro-ku, Tokyo 152-8551

⁴*The Institute of Space and Astronautical Science (ISAS),*
Japan Aerospace Exploration Agency (JAXA),
3-1-1 Yoshinodai, Sagamihara, Kanagawa 229-8510

(Received 2005 April 27; accepted 2005)

Abstract

We discuss the detectability of Warm/Hot Intergalactic medium (WHIM) via the absorption lines toward bright point sources with a future X-ray satellite mission, *XEUS*. While we consider bright QSOs as specific examples, the methodology can be applied to bright gamma-ray burst afterglows. We create mock absorption spectra for bright QSOs (more than 20 QSOs over the all sky) using a light-cone output of a cosmological hydrodynamic simulation. We assume that WHIM is under collisional and photo-ionization equilibrium. If WHIM has a constant metallicity of $Z = 0.1Z_{\odot}$, approximately 2 OVII absorption line systems with $> 3\sigma$ will be detected on average along a random line-of-sight toward bright QSOs up to $z = 0.3$ for a 30ksec exposure.

Key words: cosmology: miscellaneous — X-rays: general — methods: numerical

1. Introduction

More than 50 percent of cosmic baryons is dark (Fukugita, Hogan, & Peebles 1998; Fukugita & Peebles 2004). The abundance, physical properties, and spatial distribution of such dark baryons constitute one of the most important unsolved problems in observational cosmology. Recent numerical simulations suggest that a major fraction of dark baryons takes a form of WHIM (Warm/Hot Intergalactic medium) roughly with temperature $10^5\text{K} < T < 10^7\text{K}$

and over-density $1 < \delta < 1000$ (Cen & Ostriker 1999a; Davé et al. 2001). WHIM traces the large-scale filamentary structure of mass (dark matter) distribution more faithfully than hot intracluster gas ($T > 10^7\text{K}$ typically) and galaxies both of which preferentially reside in clusters that form around the knot-like intersections of the filamentary regions (e.g., Suto et al. 2004a, 2004b; Kang et al. 2005). This implies that WHIM carries important cosmological information in a complementary fashion to distributions of galaxies in optical and of clusters in X-ray.

DIOS (Diffuse Intergalactic Oxygen Surveyor) is a dedicated soft X-ray mission which aims at unveiling dark baryons in the universe (Ohashi et al. 2004) via oxygen emission from WHIM. Detectability of such emission features was examined in detail both for mock blank survey (Yoshikawa et al. 2003; hereafter Paper I) and for mock targeted survey of outskirts of clusters in the local universe (Yoshikawa et al. 2004; hereafter Paper II). These authors find that approximately 20 percent of cosmic baryons leaves emission signatures detectable by *DIOS*. This fraction corresponds to a relatively higher temperature tail ($10^6\text{K} < T < 10^7\text{K}$) of the entire WHIM distribution, and is sensitive to the assumed metallicity of WHIM. They adopt a metallicity model proposed by Cen & Ostriker (1999b) and Aguirre et al. (2001), but the metallicity of WHIM is admittedly very uncertain at this moment.

Another complementary strategy of detecting elusive WHIM is to search for its absorption signatures. In fact, several independent groups reported successful detections of absorption lines of highly ionized metals in spectra of background QSOs and clusters; OVII and OVIII (Fang, Bryan, Canizares 2002), OVI at $z \sim 0.2$ in the *FUSE* spectrum of QSO H1821+643 (Tripp, Savage & Jenkins 2000), and more recently O VII, N VII and NVI along the line of sight toward the Blazar Mkn 421 (Nicastro et al. 2005a; Nicastro et al. 2005b). See also Nicastro et al. (2002); Fang et al. (2002); Mathur et al. (2003); Fujimoto et al. (2004). In particular Nicastro et al. (2005a) estimate $\Omega_b^{\text{WHIM}} = (2.7^{+3.8}_{-1.9}\%) \times 10^{-[\text{O}/\text{H}]-1}$ adopting a temperature of $10^{6.1}\text{K}$ for the WHIM, where $10^{[\text{O}/\text{H}]-1}$ is the oxygen-to-hydrogen number density ratio in units of 0.1 times the solar value. While the above value seems to be in good agreement with that expected from the previous simulations (Cen & Ostriker 1999a; Davé et al. 2001), the estimate is still sensitive to the assumed temperature and metallicity of the WHIM along the single line of sight to Mkn 421 even apart from its limited statistics.

This paper examines the detectability of WHIM via absorption, instead of emission, lines using the same cosmological hydrodynamic simulation data as Paper I. In particular we consider QSOs as a bright X-ray lighthouse, and create mock absorption spectra for a future X-ray satellite mission, *XEUS* (X-ray Evolving-Universe Spectroscopy). This methodology can be equally applied to gamma-ray burst (GRB) X-ray afterglows as first proposed by Fiore et al. (2000).

The rest of the paper is organized as follows; section 2 describes our methodology and model assumptions in computing mock transmission spectra of the QSOs through WHIM. We present examples of mock spectra and their basic statistics in §3. We discuss the detectability

of WHIM via absorption in §4 and also consider how to extract physical properties of WHIM. Finally section 5 is devoted to the conclusions of the paper and to further discussion.

2. Creating Mock Transmission Spectra of WHIM toward QSOs from Cosmological Hydrodynamic Simulations

We compute mock transmission spectra of WHIM using the same simulation data as Paper I. We create a stacked light-cone output for $0 < z < 0.3$ from the simulation data. Then we consider 6400 different line-of-sight directions, and compute mock spectra for a bright QSO taking into account the cosmic X-ray background (CXB) and UV background (UVB) for photoionization sources. Our methodology is described in the following subsections.

2.1. Cosmological Hydrodynamic Simulation

We use the data of Yoshikawa et al. (2001) who performed a simulation with a hybrid code of Particle–Particle–Particle–Mesh (PPPM) Poisson solver and smoothed particle hydrodynamics (SPH). Both dark matter and gas employ 128^3 particles within a periodic simulation cube of $L_{\text{box}} = 75h^{-1}\text{Mpc}$ per side (in comoving). They adopt a standard ΛCDM model in which the density parameter $\Omega_{\text{m}} = 0.3$, the baryon density parameter $\Omega_b = 0.015h^{-2}$, the dimensionless cosmological constant $\Omega_{\Lambda} = 0.7$, the rms density fluctuation smoothed over a scale of $8h^{-1}\text{Mpc}$, $\sigma_8 = 1.0$, and the Hubble constant in units of 100km/s/Mpc $h = 0.7$. The simulation includes the effect of radiative cooling, but the energy feedback from supernova and the UV background heating are neglected. The simulation that we used here was performed in 2000. This is why the adopted value of $\Omega_b = 0.03$ is $\sim 30\%$ smaller than more recent estimate, for instance, $\Omega_b = (0.024 \pm 0.001)h^{-2}$ (Spergel et al. 2003). In this sense our results may underestimate the real absorption signatures by the corresponding amount.

We create a light-cone output for $0 < z < 0.3$ following the procedure described in Paper I. The maximum value of $z = 0.3$ is adopted so as to ensure that the OVIII line is located in a spectrum region relatively free from the Galactic confusion (Paper I), while this may be very conservative. The output extends a $5^\circ \times 5^\circ$ region on the sky, which corresponds to the simulation boxsize at $z = 0.3$; $L_{\text{box}}/(1 + 0.3)/d_{\text{A}}(z = 0.3) \approx 5^\circ$ with $d_{\text{A}}(z)$ being the angular diameter distance at redshift z .

2.2. Calculation of Optical Depths

Consider one particular line of sight (LOS) with its unit direction vector being $\hat{\mathbf{n}}$. We divide the LOS into 5000 bins x_i ($i = 1 \sim 5000$) so that their bin width is equal in comoving scale, i.e., $x_{i+1} - x_i = d_{\text{C}}(z = 0.3)/5000$, where $d_{\text{C}}(z)$ is the comoving distance at redshift z . The gas density $\rho(x_i)$, temperature $T(x_i)$ and peculiar velocity $v_r(x_i)$ of the intergalactic medium (IGM) at the i -th bin are estimated by gathering contribution from all the simulation gas particles:

$$\rho(x_i) = \sum_{j=1}^N m W(x_i \hat{\mathbf{n}} - \mathbf{r}_j, h_j), \quad (1)$$

$$T(x_i) = \sum_{j=1}^N m \frac{T_j}{\rho_j} W(x_i \hat{\mathbf{n}} - \mathbf{r}_j, h_j), \quad (2)$$

$$v_r(x_i) = \sum_{j=1}^N m \frac{v_{r,j}}{\rho_j} W(x_i \hat{\mathbf{n}} - \mathbf{r}_j, h_j). \quad (3)$$

In the above expressions, j denotes an index for gas particles ($j = 1 \sim N$), T_j , $v_{r,j}$, \mathbf{r}_j , h_j , and ρ_j are temperature, peculiar velocity, position vector, smoothing length, and density of the j -th gas particle, and m is the mass of gas particles (independent of j). Yoshikawa et al. (2001) classify some fraction of gas particles as “galaxies” if they satisfy both the Jeans condition and the over-density criterion. Those particles are excluded from the above summation. We adopt the smoothing kernel which is identical to that employed in the simulation (Yoshikawa et al. 2001):

$$W(\mathbf{x} - \mathbf{r}, h) = \frac{1}{\pi h^3} \begin{cases} 1 - (3/2)u^2 + (3/4)u^3 & \text{if } 0 \leq u \leq 1 \\ (2 - u)^3/4 & \text{if } 1 \leq u \leq 2 \\ 0 & \text{otherwise} \end{cases}, \quad (4)$$

where $u \equiv |\mathbf{x} - \mathbf{r}|/h$.

We estimate the number density of an ionized metal A^{n+} (with charge $n+$) at the i -th bin as

$$n_{A^{n+}}(x_i) = \sum_{j=1}^N F_{A^{n+}}(T_j, \rho_j) \left(\frac{n_A}{n_H} \right)_j \frac{X}{m_p} m W(x_i \hat{\mathbf{n}} - \mathbf{r}_j, h_j), \quad (5)$$

where X is the hydrogen mass fraction (we adopt 0.755), m_p is the proton mass, and $Z_{A,j}$ and $F_{A^{n+}}(T_j, \rho_j)$ represent the metallicity of A and the ionization fraction of A^{n+} of the j -th gas particle. In most cases, we assume a constant metallicity for simplicity:

$$Z_{A,j} = 0.1 Z_{A,\odot}, \quad (6)$$

or equivalently a constant number ratio:

$$(n_A/n_H)_j = 0.1 (n_A/n_H)_\odot \quad (7)$$

independently of the time and the local density (see §3.1 below for other models).

Ionization fraction is calculated using a publicly available routine, SPEX ver. 1.10. Papers I and II have assumed collisional ionization equilibrium (CIE) for simplicity because detectable emission lines preferentially come from WHIM with relatively high density. In the absorption lines, however, lower-density WHIM may become important. So in this paper we take account of the photo-ionization effect and compute the ionization fraction of metals under the collisional and photo-ionization equilibrium (CPIE)¹. To do so, we modified the

¹ Non-equilibrium ionization effects on WHIMs have recently considered by Cen & Fang (2006) and Yoshikawa,

original SPEX source code, and added routines to calculate the photo-ionization effect. For that purpose, we have to specify the differential energy distribution of the diffuse extragalactic background radiation. We simply adopt the sum of the cosmic X-ray background and the UV background (Miyaji et al. 1998; Shull et al. 1999; Chen et al. 2003):

$$J(E) = J_{\text{CXB}}(E) + J_{\text{UV}}(E), \quad (10\text{eV} < E < 10\text{keV}), \quad (8)$$

where

$$J_{\text{CXB}}(E) = J_1 \left(\frac{E}{\text{keV}} \right)^{-0.42}, \quad (9)$$

with $J_1 = 6.626 \times 10^{-26} \text{erg cm}^{-2} \text{s}^{-1} \text{sr}^{-1} \text{Hz}^{-1} (= 1.602 \times 10^{-8} \text{erg cm}^{-2} \text{s}^{-1} \text{sr}^{-1} \text{keV}^{-1})$, and

$$J_{\text{UV}}(E) = J_2 \left(\frac{E}{13.6\text{eV}} \right)^{-1.8}, \quad (10)$$

with $J_2 = 2.4 \times 10^{-23} \text{erg cm}^{-2} \text{s}^{-1} \text{sr}^{-1} \text{Hz}^{-1} (= 5.9 \times 10^{-6} \text{erg cm}^{-2} \text{s}^{-1} \text{sr}^{-1} \text{keV}^{-1})$. At $E < 0.26 \text{keV}$, J_{UV} is the dominant component of the background radiation, while J_{CXB} dominates at a larger energy region. The resulting ionization fractions of OVII and OVIII for CIE and CPlE are plotted in Figure 1.

Finally we obtain the optical depth of the ionized metal A^{n+} along a LOS up to $z = 0.3$ as

$$\tau_{A^{n+}}(E) = \int_{z=0}^{z=0.3} n_{A^{n+}}(z) \sigma_{A^{n+}}(E') \frac{dl}{dz} dz, \quad (11)$$

where the rest-frame frequency E' is given by

$$E' = E(1+z)(1+v_r/c). \quad (12)$$

Among hundreds of resonance absorption lines for $300\text{eV} < E < 2\text{keV}$ (Verner et al. 1996), we choose 10 lines for 9 ions that are relevant in the WHIM regime (see Table 1). The absorption cross section $\sigma_{A^{n+}}(E')$ at E' is computed assuming the Doppler broadening:

$$\sigma_{A^{n+}}(E') = \sum_k \frac{\pi e^2}{m_e c} f_{k,A^{n+}} \frac{2\pi\hbar c}{\sqrt{\pi} E_k b_T} \exp \left[-\frac{c^2 (E' - E_k)^2}{b_T^2 E_k^2} \right], \quad (13)$$

where k denotes the index of different absorption lines of A^{n+} , $f_{k,A^{n+}}$ and E_k are the oscillator strength and the energy of the k -th line, and $b_T = (2k_B T/m_A)^{1/2}$ is the Doppler b -parameter (m_A is the mass of the metal A).

Here we consider the thermal broadening only. Since the natural widths of the lines of our interest are less than 0.02eV , we can safely neglect them and thus use Gaussian rather than the Voigt profile. Strictly speaking, the internal turbulence is expected to be partly incorporated in our simulation data, but may not be accurate enough. Because we are mainly

Sasaki (2006). The latter paper concluded that the detectability of WHIMs is largely unaffected by the non-equilibrium effects, although the line ratio of OVII and OVIII is systematically overestimated (see their Figures 14 and 16).

interested in unsaturated lines, the additional effect of the turbulence is not supposed to be large. Thus we decided to neglect it in the current analysis.

2.3. Mock Absorption Spectra of WHIM toward a bright QSO

Now we are in a position to compute mock absorption spectra of WHIM toward a bright QSO.

Figure 2 shows the cumulative number counts of QSOs in X-ray from ROSAT data (Brinkmann, Yuan, Siebert 1997; Yuan et al. 1998). We adopt the flux of $f(0.1 - 2.4 \text{ keV}) = 7 \times 10^{-12} \text{ erg s}^{-1} \text{ cm}^{-2}$ as our fiducial value. This value is marked in the vertical dotted line. Beyond the value, we find more than 20 QSOs with $z > 0.3$. For definiteness, we adopt the power-law spectrum as

$$F_{\text{QSO}}(E) = 1.4 \times 10^{-12} \left(\frac{E}{1 \text{ keV}} \right)^{-1.5} \text{ erg s}^{-1} \text{ cm}^{-2} \text{ keV}^{-1}. \quad (14)$$

We consider mock observations of a QSO with 30 ksec exposure. Then fluence \mathcal{F} is computed by taking account of the absorption due to Galaxy and to the intervening WHIM:

$$\mathcal{F}(E) = \mathcal{F}_0(E) \exp \left[- \sum_{A^{n+}} \tau_{A^{n+}}(E) \right] \text{ [erg/cm}^2 \text{/eV]}, \quad (15)$$

$$\mathcal{F}_0(E) = \exp[-\sigma_{\text{gal}}(E)N_H] \int_{t_i}^{t_f} F_{\text{QSO}}(E) dt \text{ [erg/cm}^2 \text{/eV]}, \quad (16)$$

where $\mathcal{F}_0(E)$ determines the observable continuum level free from the WHIM absorption. The Galactic absorption is computed using the absorption cross section $\sigma_{\text{gal}}(E)$ of Morrison & McCammon (1983) who adopt 1 solar metallicity and the neutral hydrogen column density $N_H = 3 \times 10^{20} \text{ cm}^{-2}$. The resulting Galactic extinction factor, $\exp[-\sigma_{\text{gal}}(E)N_H]$, is ≈ 0.80 at $E = 0.6 \text{ keV}$. For simplicity, we neglect the additional intrinsic absorption.

2.4. Possible application to bright GRB afterglows

The same methodology can be applied to bright GRB afterglows. In addition to its intrinsic brightness, the more important advantage of GRB for the WHIM science lies in its transient nature; once absorption lines due to WHIM are detected, one can perform deep follow-up observations to look for the emission counterpart (Papers I and II) after the GRB is completely faded. Successful detections of both absorption and emission features will offer unambiguous evidence of WHIM, although not so easy in reality.

Piro (2004) pointed out that the average spectrum energy distribution of a typical GRB afterglow is approximated as

$$F_{\text{GRB}}(t, E) = F_0 \left(\frac{t}{40000 \text{ s}} \right)^{-\delta} \left(\frac{E}{1 \text{ keV}} \right)^{-\alpha}, \quad (17)$$

$$\delta = 1.2 \pm 0.2, \quad \alpha = 1.13 \pm 0.07. \quad (18)$$

For six years between 1997 and 2002, BeppoSax observed 8% of the entire sky (Jager et al 1997). The brightest GRB afterglow detected has $F_0 = 6 \times 10^{-12} \text{ erg s}^{-1} \text{ cm}^{-2} \text{ keV}^{-1}$ approximately

(Piro 2004; De Pasquale et al. 2005).

We consider mock observations of a GRB afterglow for $t_i < t < t_f$ after the GRB event ($t = 0$). If we observe this GRB afterglow with $(t_i, t_f) = (1\text{day}, 1\text{ day} + 30\text{ksec})$, the fluence is comparable with one for our fiducial QSO. For definiteness, we adopt the flux as our fiducial value:

$$F_{\text{GRB}}(t, E) = 6 \times 10^{-12} \left(\frac{t}{40000\text{s}} \right)^{-1.2} \left(\frac{E}{1\text{keV}} \right)^{-1.13} \text{erg s}^{-1}\text{cm}^{-2}\text{keV}^{-1}. \quad (19)$$

Assuming a nominal observational efficiency of 50%, GRB afterglows brighter than our fiducial value (Eq.[19]) are roughly expected to be $\approx 1/0.5/0.08/6 = 4$ per year over the entire sky. In reality, however, the above estimate is statistically limited so far, and a better estimate will be given from the on-going *Swift* observation.

3. Results

3.1. Identification of absorption lines in mock spectra

Once mock spectra are constructed, our next task is to attempt the mock observation, and in particular, to identify absorption lines in an objective manner. For this purpose, we follow the procedure described in Fang, Bryan, Canizares (2002). Consider a schematic example of normalized absorption line profiles, $\exp(-\tau)$ as in Figure 3. We set a threshold value $F_{\text{th}} = 10^{-5}$, and identify a contiguous region below the threshold $1 - F_{\text{th}}$ as an absorption line system. Suppose the line profile which first down-crosses the $1 - F_{\text{th}}$ at $E = E_i$ and then up-crosses at $E = E_f$. The equivalent width W (in the observer's frame) of this system centered at $E = E_l$ is calculated by integrating $1 - \exp(-\tau)$ over $E_i < E < E_f$:

$$W_l(E_l) = \int_{E_i}^{E_f} [1 - e^{-\tau(E)}] dE. \quad (20)$$

If the line system is identified as a particular species with the oscillator strength f_l , the equivalent width in its unsaturated regime is rewritten in terms of the corresponding column density N_l as:

$$N_l = \frac{9 \times 10^{14}}{f_l} \frac{W_l}{0.1\text{eV}} [\text{cm}^{-2}]. \quad (21)$$

In the present case, the S/N is determined by the energy resolution of the detector (for *XEUS*, the effective area $S_{\text{eff}} = 60000\text{cm}^2$ and the energy resolution $\Delta E = 2\text{eV}$; for comparison, intrinsic widths of the lines of our interest are typically below 1 eV). Therefore the S/N at the energy of the line center, E_l , is estimated as

$$S/N(E_l) = \frac{[\mathcal{N}_0(E_l) - \mathcal{N}(E_l)]\Delta E}{\sqrt{\mathcal{N}(E_l)\Delta E}} \quad (22)$$

simply from the Poisson statistics of the observed photons, where \mathcal{N} and \mathcal{N}_0 are the photon number counts [ph/eV] with absorption and without absorption (continuum level), respectively.

We compute the equivalent width and the S/N of absorption line systems for 6400 random LOSs in the $5^\circ \times 5^\circ$ region assuming the fluence described in §2.3. Figure 4 plots the cumulative number distribution of the equivalent width of absorption line systems per LOS ($z = 0.0 - 0.3$) from our mock observation for 10 strong lines (Table 1). On average, O VII (574 eV) is the most prominent line in terms of the equivalent width, and O VIII (654 eV) and Fe XVII (826 eV) are the next. Figure 5 shows the corresponding cumulative number distribution of S/N . Note that the value of S/N should be replaced by

$$\begin{aligned} S/N &= (S/N)_{\text{fiducial}} \left(\frac{F_0}{6 \times 10^{-12} [\text{erg s}^{-1} \text{cm}^{-2} \text{keV}^{-1}]} \right)^{1/2} \\ &= (S/N)_{\text{fiducial}} \left(\frac{\mathcal{N}_0(E = 500 \text{eV})}{8800 [\text{ph/eV}]} \right)^{1/2} \end{aligned} \quad (23)$$

if F_0 , and more generally the number of photons during the exposure time, \mathcal{N}_0 , are different from our fiducial values. In our adopted model for the QSO and the *XEUS* performance, O VII 574 eV and OVIII 654 eV lines achieve $S/N = 3$ when their equivalent widths are $W = 0.05$ eV. We take this value as our detection limit.

We find that the number of absorption systems which have $S/N \geq 3$ is 1.58/LOS (OVII 574 eV) and 0.37/LOS (O VIII 654 eV) as summarized in Table 2. The other eight lines exhibit below 0.1 systems/LOS. The number of the case that both OVII (574 eV) and OVIII (654 eV) exhibit $S/N \geq 3$ at the same position of WHIM is 0.35/LOS.

In order to check the dependence on the assumed metallicity model, we also consider two other metallicity models. One is a phenomenological model adopted in Paper II (the radiation pressure ejection model of Aguirre et al. 2001):

$$Z_{A,j}/Z_{A,\odot} = \min [0.2, 0.02(\rho_j/\bar{\rho}_b)^{0.3}], \quad (24)$$

where $\bar{\rho}_b$ is the mean baryon density at redshift z . The other adopts a constant metallicity comparable to the typical value for intra-cluster medium:

$$Z_{A,j} = 0.3Z_{A,\odot}. \quad (25)$$

Figure 6 shows the dependence of the cumulative number distribution of oxygen absorption line systems on the metallicity models; O VII (574eV) and O VIII (654eV) in thick and thin lines, respectively. Note that $Z_{A,j} > 0.1Z_{A,\odot}$ is satisfied only in relatively dense regions $\rho_j/\bar{\rho}_b > 214$ (eq.[24]). This is why our fiducial model ($Z_{A,j} = 0.1Z_{A,\odot}$) has more absorption line systems than the model of equation (24).

We also show the results toward our fiducial GRB afterglow in Table 3. These are almost equivalent to those toward our fiducial QSO (Table 2). Thus, we concentrate on the results toward QSOs in what follows.

3.2. Detectability of Oxygen Absorption Line Systems

Since the most prominent absorption lines detectable by *XEUS* are OVII and OVIII, we focus on these lines in what follows. Figure 7 shows column density maps of OVII (*Left panel*) and OVIII (*Right panel*) for $0 < z < 0.3$. As indicated in those panels, we select three different LOSs (A, B, and C). The mock spectra for those LOSs are shown in Figure 8; spectrum A exhibits many prominent absorption lines, and spectrum B has one strong line system while spectrum C has none.

We find two distinct absorption line systems which are located at $z = 0.12$ (marked by †) and $z = 0.29$ (marked by ‡) along the LOS of A; OVII ($z = 0.29$, $E = 445\text{eV}$, $W = 0.16\text{eV}$), OVIII ($z = 0.29$, $E = 507\text{eV}$, $W = 0.09\text{eV}$), OVII ($z = 0.12$, $E = 514\text{eV}$, $W = 0.10\text{eV}$), and OVIII ($z = 0.12$, $E = 585\text{eV}$, $W = 0.12\text{eV}$). Figure 9 plots the column density map of OVII (*Left panels*) and OVIII (*Right panels*) but for $0.11 < z < 0.14$ (*Upper panels*) and for $0.26 < z < 0.30$ (*Lower panels*) so as to depict the WHIM responsible for the absorption systems in the spectrum A.

Figure 10 shows the mass-weighted (within each cell) temperature and the over-density distributions along the three LOSs. The top two panels for the region A have high over-density (10-100) and high temperature ($10^6 - 10^7\text{K}$) WHIM clumps at $z = 0.12$ and $z = 0.29$. They are indeed responsible for the prominent lines in the spectrum A of Figure 8. Spectrum B has one absorption system at $z = 0.22$ (OVII 574 eV $W = 0.06\text{eV}$) as indicated in Figures 9 and 10. In reality, however, the identification of the line redshift is very difficult from a single line alone. One may assume statistically that the strongest line in a single LOS should be that of OVII 574 eV, and then infer the redshift $574/470 - 1 = 0.22$. In this particular example, it turns out a correct guess, but may not work always. Finally spectrum C has no prominent absorption feature. Indeed Figure 10 shows that there is no region with over-density $\delta \equiv \rho/\bar{\rho} > 10$ along the LOS.

Figure 11 plots the distributions of mass-weighted temperatures and over-densities of WHIM averaged over each absorption line system of OVII (574 eV) and O VIII (654 eV). Spatial boundaries of absorption line systems are somewhat ambiguous. We define here the cosmic mean density as the threshold as illustrated in Figure 12, and we identify one connected region exceeding $\delta = 1$ as a single absorption system even if there are many density peaks and valleys inside. Then we compute its temperature and over-density by mass-weighted averaging over the relevant SPH particles within the entire line system.

The different symbols indicate the range of the equivalent width W of the absorption line systems; circles, crosses and triangles correspond to the systems with $W \geq 0.12\text{ eV}$, $0.07 \leq W \leq 0.12\text{ eV}$, and $0.05 \leq W \leq 0.07\text{ eV}$, respectively. Both OVII and O VIII can probe WHIM with $T > 10^6 - 10^7\text{ K}$ and over-density of $\delta = 10$ to 1000. WHIM with $T < 10^6\text{ K}$, however, can be traced only by O VII.

Figure 13 plots the fraction of gas contained in oxygen absorption line systems (O VII in *Left panels* and O VIII in *Right panels*) which have the equivalent width larger than the

specified value W . In practice we first select all oxygen absorption line systems along the i -th LOS whose equivalent width exceeds W , and sum up their hydrogen gas column densities. We denote the sum as $N_{H,i}^{\text{sim}}(> W)$. Then we take the following ratio averaged over 6400 LOSs:

$$R_H(> W) = \frac{\sum_{i=1}^{6400} N_{H,i}^{\text{sim}}(> W)}{\sum_{i=1}^{6400} N_{H,i}^{\text{sim}}(> 0)} \quad (26)$$

for O VII and O VIII separately. In reality this is an *unobservable* quantity, but provides a *simulated* gas mass fraction of oxygen absorption line systems which have a detectable line width. More importantly, this is the essential factor in properly estimating the total cosmic baryon density from the detected fraction of oxygens (§4.2).

In the upper panels, three shaded regions correspond to the temperature ranges $T > 10^7$ K, $10^6 < T < 10^7$ K, and $T < 10^6$ K from top to bottom, and in the lower panels, three shaded regions correspond to the density contrast ranges $\delta > 100$, $10 < \delta < 100$, $\delta < 10$ from top to bottom. Comparison of the left and right panels suggests that OVIII traces higher temperature and denser regions than O VII. In the case of O VII (574 eV), we can detect only 32 % of baryon above the detection limit ($W \sim 0.05$ eV; §3.1). The region of $T > 10^7$ K accounts for 19 % of detectable baryons, which may be located in virialized regions like intra-cluster medium and thus may be already detected through their thermal bremsstrahlung. The regions of $10^6 < T < 10^7$ K and $T < 10^6$ K account for 68 % and 12 % of detectable baryons, which can be regarded as WHIM. Note that one can detect the absorption lines of O VII (574eV) with $T < 10^6$ K, while it is almost impossible to find their emission counterparts (Paper I).

4. Physical Properties of the identified WHIM

4.1. OVII and OVIII Absorption Lines

As we have seen, the most prominent absorption lines are OVII (574 eV) and OVIII (654 eV). On average, 35 % of random LOSs have an intervening clump of WHIM which exhibits both absorption lines with $S/N \geq 3$. In this case, the ratio of their equivalent widths should provide the temperature of the WHIM *in principle*. Consider a clump of WHIM which has a uniform temperature T and density ρ , then the ratio of the equivalent widths for unsaturated lines that are relevant here is written as

$$\frac{W_{\text{OVII},574\text{eV}}}{W_{\text{OVIII},654\text{eV}}} \sim \frac{f_{\text{OVII},574\text{eV}} F_{\text{OVII}}(T, \rho)}{f_{\text{OVIII},654\text{eV}} F_{\text{OVIII}}(T, \rho)}, \quad (27)$$

where f is the oscillator strength and F is the ionization fraction. The WHIM which exhibits OVIII (654 eV) absorption has temperature of $10^6 - 10^7$ K (Figure 11). In this temperature range, the ionization fraction approaches the value in CIE, and the ratio of the oxygen equivalent widths, eq.(27), is expected to be insensitive to the density, ρ .

Figure 14 provides the scatter plot of the ratio of O VII and O VIII equivalent width versus the mass-weighted average temperature for systems where both O VII (574 eV) and O VIII (654 eV) exhibit $S/N \geq 3$. Three solid lines indicate the theoretical curves in Eq. (27) applying different hydrogen number density $n_H = 10^{-5}$, 10^{-6} , and 10^{-7} cm^{-3} from top to bottom. Inhomogeneous density and temperature structures are responsible for the departure from the theoretical model which assumes uniform distribution. Figure 15 shows an example of sub-structure in a simulated absorption line system. Temperature is the highest near the center of the clump, and over-density is also high. Therefore, ionization fractions of OVII and OVIII are rather suppressed. This anti-correlation of oxygen abundances inside the inhomogeneous distribution of WHIMs explains why the simulated systems in Figure 14 preferentially lie at higher temperature regime than the theoretical prediction.

4.2. Estimating Ω_b from WHIM observations

If absorption lines of WHIM are detected along a particular line of sight, one would naturally attempt to estimate the contribution of WHIM to the total cosmic baryon density, Ω_b^{WHIM} . Nicastro et al. (2005a) indeed reported $\Omega_b^{\text{WHIM}} = (2.7^{+3.8}_{-1.9}\%) \times 10^{-[\text{O}/\text{H}]-1}$ using two OVII absorption lines. We perform statistical analysis of Ω_b^{WHIM} estimation using our mock data.

Let us first define the estimated fraction of WHIM with signal-to-noise ratio exceeding a given threshold, S/N , along one LOS as follows:

$$\Omega_{\text{gas}}^{\text{WHIM,est}}(> S/N) = \frac{1}{d_c(z=0.3)\rho_c} \sum_i \frac{N_{H,i}^{\text{est}}(> S/N)}{X(1+z_i)^2}, \quad (28)$$

$$N_{H,i}^{\text{est}}(> S/N) = \frac{N_{\text{OVII},i}(> S/N)}{F_{\text{OVII},i}(T)} \left(\frac{n_H}{n_O} \right) \quad (29)$$

where i denotes an index for absorption line systems, $X (= 0.755)$ is the hydrogen mass fraction, and $d_c(z=0.3)$ is the comoving distance from $z=0$ to $z=0.3$. We convert the observed equivalent width into $N_{\text{OVII}}(> S/N)$ using Eq. (21) assuming that the line is unsaturated, i.e., in its linear regime of the growth curve. At present, no simultaneous detection of OVII and OVIII absorption lines in WHIM is reported. Consider first, however, the case in which both O VII and O VIII are detected. Then we estimate temperature T using Eq. (27) and derive the ionization fraction $F_{\text{OVII}}(T)$ assuming collisional ionization equilibrium. If we multiply the hydrogen-to-oxygen number ratio, we have an estimate of the hydrogen column density for the i -th absorption line system, $N_{H,i}^{\text{est}}(> S/N)$. In practice, we adopt $(n_O/n_H) = 0.1(n_O/n_H)_\odot = 10^{-4.07}$ (Anders & Grevesse 1989). Finally this is converted to the density parameter of gas, $\Omega_{\text{gas}}^{\text{WHIM,est}}(> S/N)$ responsible for absorption exceeding the detection S/N .

As we have seen in the previous sections, the inhomogeneity of the temperature and density within one absorption system would result in a systematic underestimate of $N_{H,i}^{\text{est}}(> S/N)$. In order to check the systematic effect as well as the assumption of CIE in equation (29) (while we did adopt CPlE in creating mock spectra from simulation data), we compare

$N_{H,i}^{\text{est}}(> S/N)$ with $N_{H,i}^{\text{sim}}(> S/N)$ directly computed from simulation data (§3.2). Figure 16 clearly shows the degree of the underestimate bias.

In order to estimate the total baryon density, Ω_b^{est} , from $\Omega_{\text{gas}}^{\text{WHIM,est}}(> S/N)$, we have to correct for (i) the fraction of gas below the detection limit, (ii) the fraction of stars in galaxies, and (iii) the above systematic bias. Therefore we write the estimate as

$$\Omega_b^{\text{est}} = \frac{\Omega_{\text{gas}}^{\text{WHIM,est}}(> S/N)}{R_H(> S/N)} \frac{f_{\text{gas}} + f_{\text{star}}}{f_{\text{gas}}} \left\langle \frac{N_H^{\text{sim}}(> S/N)}{N_H^{\text{est}}(> S/N)} \right\rangle. \quad (30)$$

In practice, we choose $S/N = 3$ in the following. We compute the fraction of WHIMs which exhibit both OVII and OVIII absorptions (similarly as in Figure 13), and find $R_H(> 3\sigma) = 0.22$. As for the second factor, we evaluate directly from simulations; $f_{\text{gas}} = 0.79$ and $f_{\text{star}} = 0.21$. As Figure 16 indicates, the last correction factor significantly varies from line to line, and it is not easy to choose a relevant average value. If we adopt the mean value as plotted in triangles, $\langle N_H^{\text{sim}}(> 3\sigma)/N_H^{\text{est}}(> 3\sigma) \rangle \sim 1/4$. Adopting those correction factors, we plot the histogram of Ω_b^{est} in Figure 17.

Upper panel is the case where both OVII and OVIII absorptions are detected (1903 LOSs out of 6400 LOSs). The mean value of the resulting Ω_b^{est} averaged over the entire LOSs (even including the non-detected 4097 LOSs) amounts to 0.023 (plotted in the dotted line). This is in reasonable agreement with the value adopted in the simulation, 0.03. On the other hand, it clearly demonstrates the fact that any estimate based on the positive detection alone may significantly overestimate the real value; it is essential to take account of the above correction factors properly.

Lower panel in Figure 17 indicates the 5217 LOSs along which only O VII absorption lines are detected. In this case, one has to assume the temperature *a priori*, and we show results for $T = 10^{5.5}$, $10^{6.0}$, and $10^{6.5}$ K. The temperature dependence is very strong and even not monotonic. This reflects the strong dependence of OVII fraction on temperature as exhibited in Figure 1. The two peaks in the histogram correspond to LOSs which have single and double absorption line systems. If we assume $T = 10^6$ K (the ionization fraction of OVII peaks around this temperature), OVII absorption lines alone provides a fairly accurate estimate for Ω_b (Nicastro et al. 2005a).

5. Conclusions and Discussion

In this paper, we have examined the detectability of WHIM via the absorption lines in a bright QSO spectra using the cosmological hydrodynamic simulation. We created the mock *XEUS* absorption spectra toward a bright QSO assuming the collisional and photo-ionization equilibrium. We conclude that on average *XEUS* will detect 1.58 (O VII 574 eV) and 0.37 (OVIII 654 eV) per a random line-of-sight up to $z = 0.3$ ($S/N \geq 3$).

If both OVII and OVIII absorptions are detected ($\sim 40\%$ chance) for the same WHIM clump, one can estimate its temperature from their line ratios and attempt to infer the cosmic

baryon density. As we discussed in detail, however, the reliable estimate requires several careful correction factors and still the resulting distribution function of the estimate is fairly wide. So any attempt on the basis of small statistical samples should be interpreted with caution.

In passing we have to emphasize once again that our simulation data adopted $\Omega_b = 0.03$ rather than the currently more favored value 0.04. Also we restrict our current analysis up to $z = 0.3$ where a spectrum is relatively free from the Galactic confusion, but in principle one can explore WHIM systems at higher redshifts ($z \sim 1$) with QSO(GRB). Therefore while our present conclusions concerning the detectability of WHIM in absorption toward a QSO(GRB) may seem fairly modest, most likely they are very conservative. Moreover the result is very sensitive to the metallicity of WHIM which is rather uncertain and is likely to significantly vary from place to place. Given the strong metallicity dependence as shown in Figure 6, what is relevant is not the mean metallicity of WHIM but the fraction of WHIM clumps which exhibit detectable equivalent width. In this respect, the wide variation of the metallicity, even if its overall mean is $0.1Z_\odot$ as we most adopted here, is expected to *systematically* increase the detectability.

Throughout this paper, we adopted $\Delta E = 2\text{eV}$ with calorimeter on-board *XEUS* in mind. Current observations of WHIM by several grating detectors are indicative. With *XEUS*'s large effective area, WHIM absorption features will be collected with a much larger number of samples as a by-product of QSO studies. With careful statistical studies as we presented in this paper, these significantly contribute to the proper understanding of physics of WHIM. If higher energy resolution with gratings, for example, $\Delta E = 0.15\text{eV}$ at $E = 0.6\text{keV}$, becomes available in future, it is even possible to obtain line profile accurately and estimate the effect of turbulence. Also one can study multiphase nature in a single absorption system. Furthermore, since signal-to-noise ratio improves as $1/\sqrt{\Delta E}$, one can significantly increase the number of detectable oxygen and other ion absorption systems. These significantly contribute to the proper understanding of physics of WHIM (Nicastro 2005).

In order to be more quantitative, we need much more advanced simulation datasets which include more realistic physical processes such as radiative cooling, photo-ionization, star formation, supernova feedback, and metallicity evolution. This is exactly what we are performing, and we hope to revisit the above issues in due course.

Numerical computations presented in this paper were carried out at ADAC (the Astronomical Data Analysis Center) of the National Astronomical Observatory, Japan (project ID: mky05a). We thank the referee Fabrizio Nicastro for very constructive and useful comments. We believe that his numerous suggestions significantly improve the present paper. We are also grateful to Kei Hiraki and Mari Inaba for their generous allocation of computer resources at the University of Tokyo supported by the Special Coordination Fund for Promoting Science and Technology, Ministry of Education, Culture, Sport, Science and Technology. This work was supported in part by Grants-in-Aid for Scientific Research from the Japan Society

for Promotion of Science (Nos.14102004, 14204017, 15340088, 15740157, and 16340053).

References

- Aguirre, A., Hernquist, L., Schaye, J., Katz, N., Weinberg, D.H., & Gardner, J. 2001, ApJ, 561, 521
- Anders, E., & Grevesse, N. 1989, Geochim. Cosmochim. Acta, 53, 197
- Brinkmann, W., Yuan, W., & Siebert, J. 1997, A&A, 319, 413
- Cen, R. & Fang, T. 2006, ApJ, submitted (astro-ph/0601009)
- Cen, R. & Ostriker, J. 1999a, ApJ, 514, 1
- Cen, R. & Ostriker, J. 1999b, ApJ, 519, L109
- Chen, X., Weinberg, D.H., & Davé, R. 2003, ApJ, 594, 42
- Davé, R., Cen, R., Ostriker, J.P., Bryan, G.L., Hernquist, L., Katz, N., Weinberg, D.H., Norman, M.L., & O’Shea, B. 2001, ApJ, 552, 473
- De Pasquale, M., Piro, L., Gendre, B., Amati, L., Antonelli, L.A., Costa, E., Feroci, M., Frontera, F., Nicastro, L., Soffitta, P., & in’t Zand, J. 2005, astro-ph/0507708
- Fang, T., Bryan, G.L., & Canizares, C.R. 2002, ApJ, 564, 604
- Fang, T., Marshall, H.L., Lee, J.C., Davis, D.S., & Canizares, C.R., 2002, ApJ, 572, L127
- Fiore, F., Nicastro, F., Savaglio, S., Stella, L., & Vietri, M., 2000, ApJ, 544, L7
- Fukugita, M., Hogan, C.J., & Peebles, P.J.E. 1998, ApJ, 503, 518
- Fukugita, M., & Peebles, P.J.E. 2004, ApJ, 616, 643
- Fujimoto, R., Takei, Y., Tamura, T., Mitsuda, K., Yamasaki, N.Y., Shibata, R., Ohashi, T., Ota, N., Audley, M.D., Kelley, R.L., Kilbourne, C.A., 2004, PASJ, 56, L29
- Jager, R., Mels, W. A., Brinkman, A. C., Galama, M. Y., Goulooze, H., Heise, J., Lowes, P., Muller, J. M., Naber, A., Rook, A., Schuurhof, R., Schuurmans, J. J., Wiersma, G., 1997, A&A S, 125, 557
- Kang, H., Ryu, D., Cen, R., Song, D., 2005, ApJ, 620, 21
- Morrison R. & McCammon D., 1983, ApJ, 270, 119
- Miyaji, T., Ishisaki, Y., Ogasaka, Y., Ueda, Y., Freyberg, M. J., Hasinger, G., & Tanaka, Y. 1998, A&A, 334, 13
- Mathur, S., Weinberg, D.H., & Chen, X. 2003, ApJ, 582, 82
- Nicastro, F. 2005, talk presented at an international workshop on *Measuring the Diffuse Intergalactic Medium*, Kanagawa, Japan.
- Nicastro, F., Zezas, A., Drake, J., Elvis, M., Fiore, F., Fruscione, A., Marengo, M., Mathur, S., & Bianchi, S. 2002, ApJ, 573, 157
- Nicastro, F., Mathur, S., Elvis, M., Drake, J., Fang, T., Fruscione, A., Krongold, Y., Marshall, H., Williams, & R., Zezas, A. 2005a, Nature, 433, 495
- Nicastro, F., Mathur, S., Elvis, M., Drake, J., Fiore, F., Fang, T., Fruscione, A., Krongold, Y., Marshall, H., & Williams, R. 2005b, ApJ, 629, 718
- Ohashi, T. et al., 2003, in Proceedings of “Modelling the Intergalactic and Intracluster Media” (astro-ph/0402546)
- Piro, L., 2004, in Proceedings of “Third Rome Workshop on Gamma-Ray Bursts in the Afterglow Era” (astro-ph/0402638)

- Shull, J.M., Roberts, D., Giroux, M.L., Penton, S.V., & Fardal, M.A. 1999, AJ, 118, 1450
- Spergel, D. N. et al. 2003, ApJS, 148, 175
- Suto, Y., Yoshikawa, K., Yamasaki, N.Y., Mitsuda, K., Fujimoto, R., Furusho, T., Ohashi, T., Ishida, M., Sasaki, S., Ishisaki, Y., Tawara, Y., Furuzawa, A. 2004a, Journal of the Korean Physical Society, 45, S110
- Suto, Y., Yoshikawa, K., Dolag, K., Sasaki, S., Yamasaki, N.Y., Ohashi, T., Mitsuda, K., Tawara, Y., Fujimoto, R., Furusho, T., Furuzawa, A., Ishida, M., Ishisaki, Y., Takei, Y. 2004b, Journal of the Korean Astronomical Society, 37, 387
- Tripp, T.M., Savage, B.D., & Jenkins, E.B. 2000, ApJ, 534, L1
- Verner, D.A., Verner, E.M., & Ferland, G.J. 1996, Atomic Data Nucl. Data Table, 64, 1
- Yoshikawa, K., Taruya, A., Jing, Y.P., & Suto, Y. 2001, ApJ, 558, 520
- Yoshikawa, K., Yamasaki, N.Y., Suto, Y., Ohashi, T., Mitsuda, K., Tawara, Y., Furuzawa, A. 2003, PASJ, 55, 879 (Paper I)
- Yoshikawa, K., Dolag, K., Suto, Y., Sasaki, S., Yamasaki, N.Y., Ohashi, T., Mitsuda, K., Tawara, Y., Fujimoto, R., Furusho, T., Furuzawa, A., Ishida, M., Ishisaki, Y., & Takei, Y. 2004, PASJ, 56, 939 (Paper II)
- Yoshikawa, K., & Sasaki, S. 2006, PASJ in press. (astro-ph/060372)
- Yuan, W., Brinkmann, W., Siebert, J., & Voges, W. 1998, A&A, 330, 108

Table 1. Ten prominent resonant absorption lines in 0.3 – 2.0 keV

species	energy	oscillator strength
CVI	368 eV	0.416
NVI	431 eV	0.675
NVII	500 eV	0.416
OVI	574 eV	0.696
OVI	666 eV	0.146
OVIII	654 eV	0.416
NeIX	922 eV	0.724
NeX	1022 eV	0.416
MgXI	1352 eV	0.742
FeXVII	826 eV	2.96

Table 2. Expected number of oxygen absorption line systems with $S/N \geq 3$ and $S/N \geq 2$ per LOS up to $z = 0.3$ toward a QSO discussed in §2.3.

metallicity model		expected number/LOS		
		OVI (574 eV)	OVIII (654 eV)	OVI and OVIII
$Z = 0.1Z_{\odot}$	$S/N \geq 3$	1.58	0.37	0.35
	$S/N \geq 2$	3.07	0.82	0.79
$Z = \min[0.2, 0.02(\rho/\bar{\rho})^{0.3}]Z_{\odot}$	$S/N \geq 3$	0.50	0.15	0.14
	$S/N \geq 2$	0.97	0.31	0.28
$Z = 0.3Z_{\odot}$	$S/N \geq 3$	6.71	2.19	2.10
	$S/N \geq 2$	9.91	3.40	3.22

Table 3. Expected number of oxygen absorption line systems with $S/N \geq 3$ and $S/N \geq 2$ per LOS up to $z = 0.3$ toward a GRB afterglow discussed in §2.4.

metallicity model		expected number/LOS		
		OvII (574 eV)	OvIII (654 eV)	OvII and OvIII
$Z = 0.1Z_{\odot}$	$S/N \geq 3$	1.71	0.43	0.41
	$S/N \geq 2$	3.30	0.94	0.90
$Z = \min[0.2, 0.02(\rho/\bar{\rho})^{0.3}]Z_{\odot}$	$S/N \geq 3$	0.55	0.17	0.15
	$S/N \geq 2$	1.05	0.35	0.32
$Z = 0.3Z_{\odot}$	$S/N \geq 3$	7.08	2.39	2.28
	$S/N \geq 2$	10.3	3.66	3.45

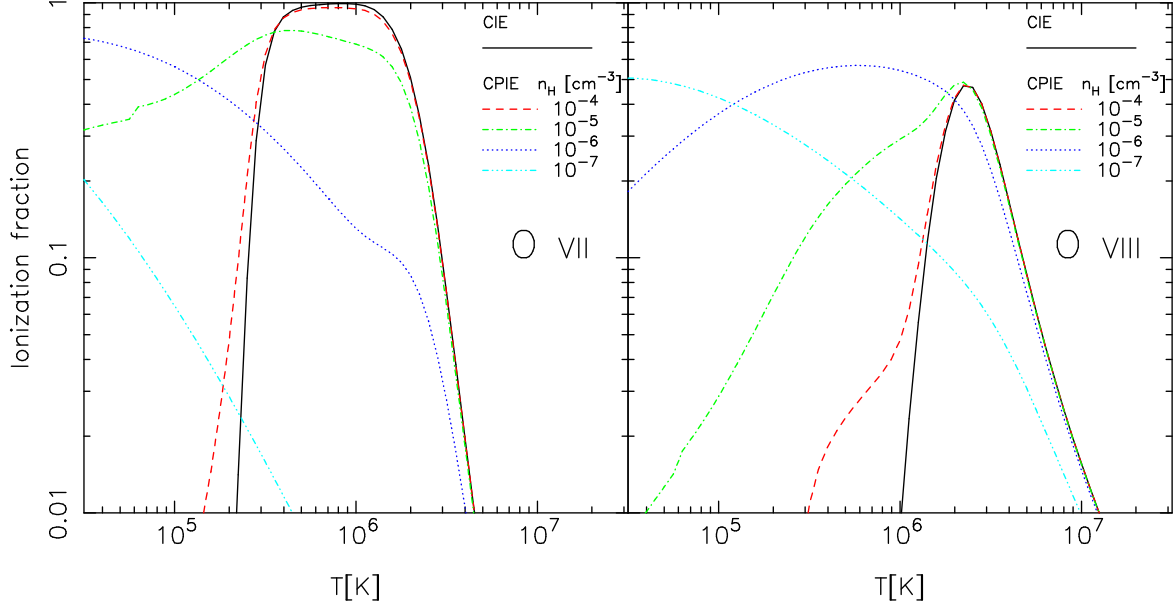


Fig. 1. Ionization fractions of OVII and OVIII as a function of temperature. Solid lines represent results for CIE (Collisional Ionization Equilibrium), while other different lines indicate those for C PIE (Collisional and Photo-Ionization Equilibrium) adopting the hydrogen number density $n_H = 10^{-4}$, 10^{-5} , 10^{-6} , and 10^{-7} cm^{-3} .

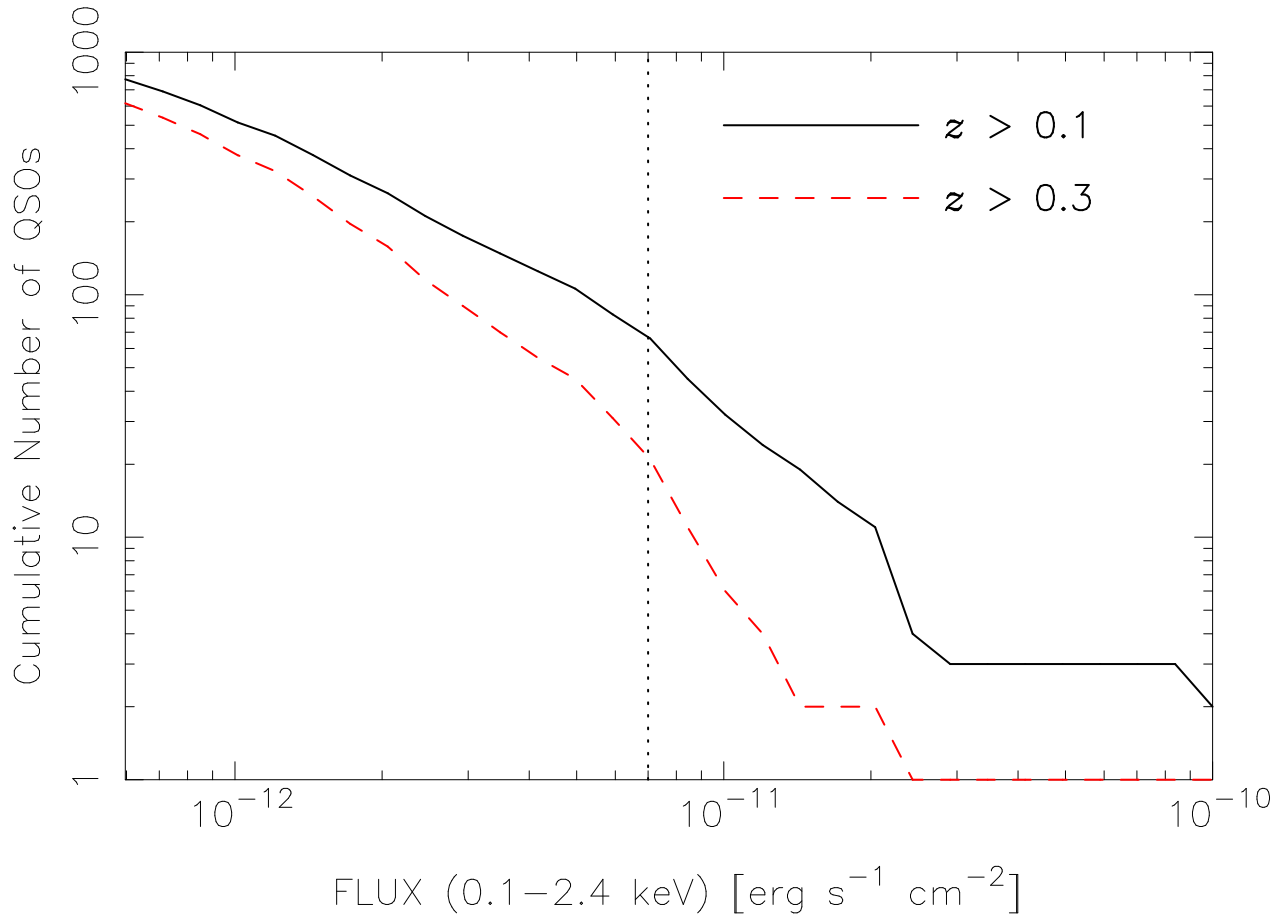


Fig. 2. Cumulative number counts of QSOs in X-ray from ROSAT data as a function of their 0.1 – 2.4 keV flux. Solid and dashed lines indicate QSOs with $z > 0.1$ and $z > 0.3$, respectively.

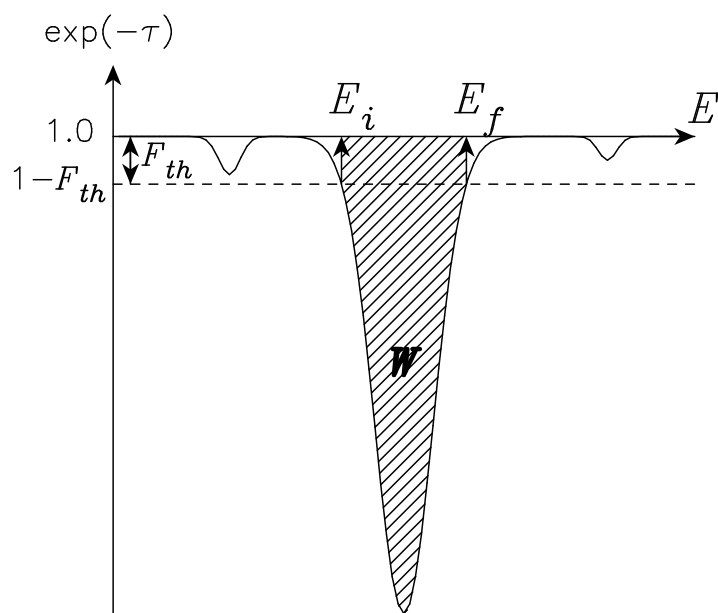


Fig. 3. Schematic identification method of absorption lines.

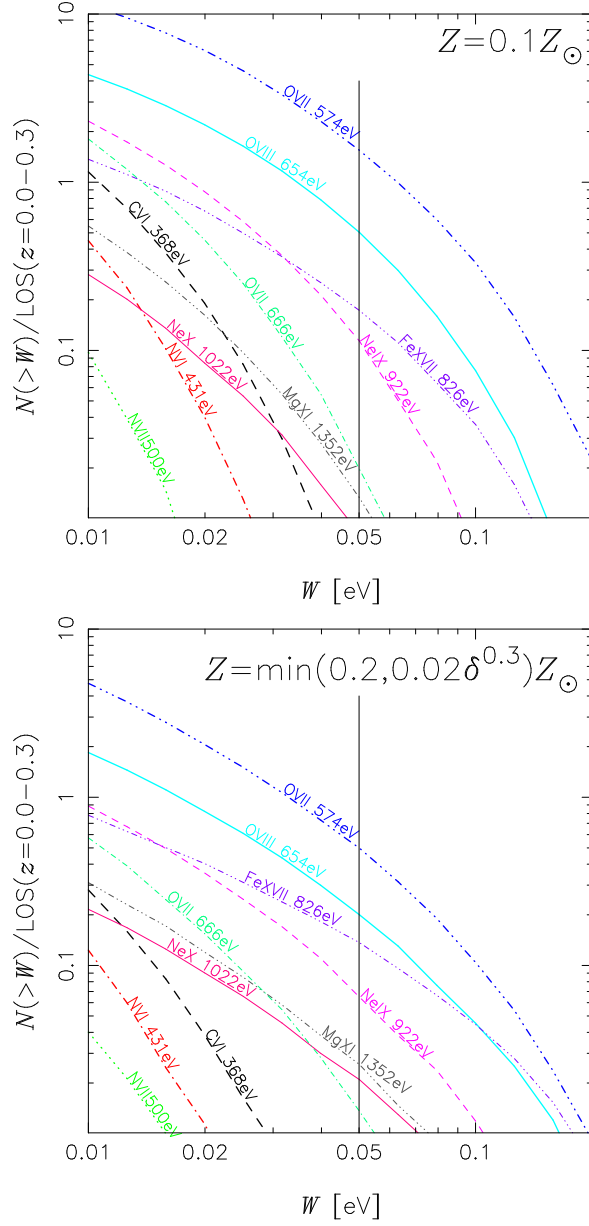


Fig. 4. Cumulative distribution of expected number of absorption line systems for $0 < z < 0.3$ as a function of their equivalent width; *Upper panel:* $Z = 0.1 Z_{\odot}$, *Lower panel:* $Z/Z_{\odot} = \min[0.2, 0.02(\rho/\bar{\rho}_b)^{0.3}]$. Solid vertical lines indicate our fiducial detection limit for the equivalent width ($W = 0.05$ eV).

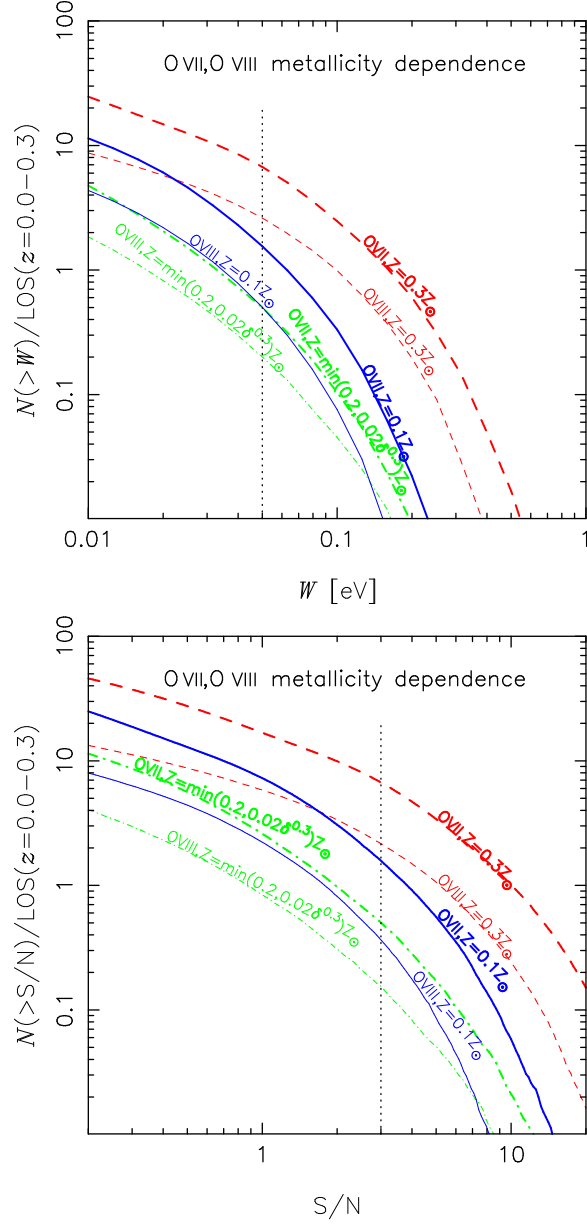


Fig. 6. Cumulative distribution of OvII and OvIII absorption lines for different metallicity models as a function of W (*Upper panel*) and S/N (*Lower panel*). Dotted vertical lines indicate our fiducial detection limits ($W = 0.05\text{eV}$ and $S/N = 3$).

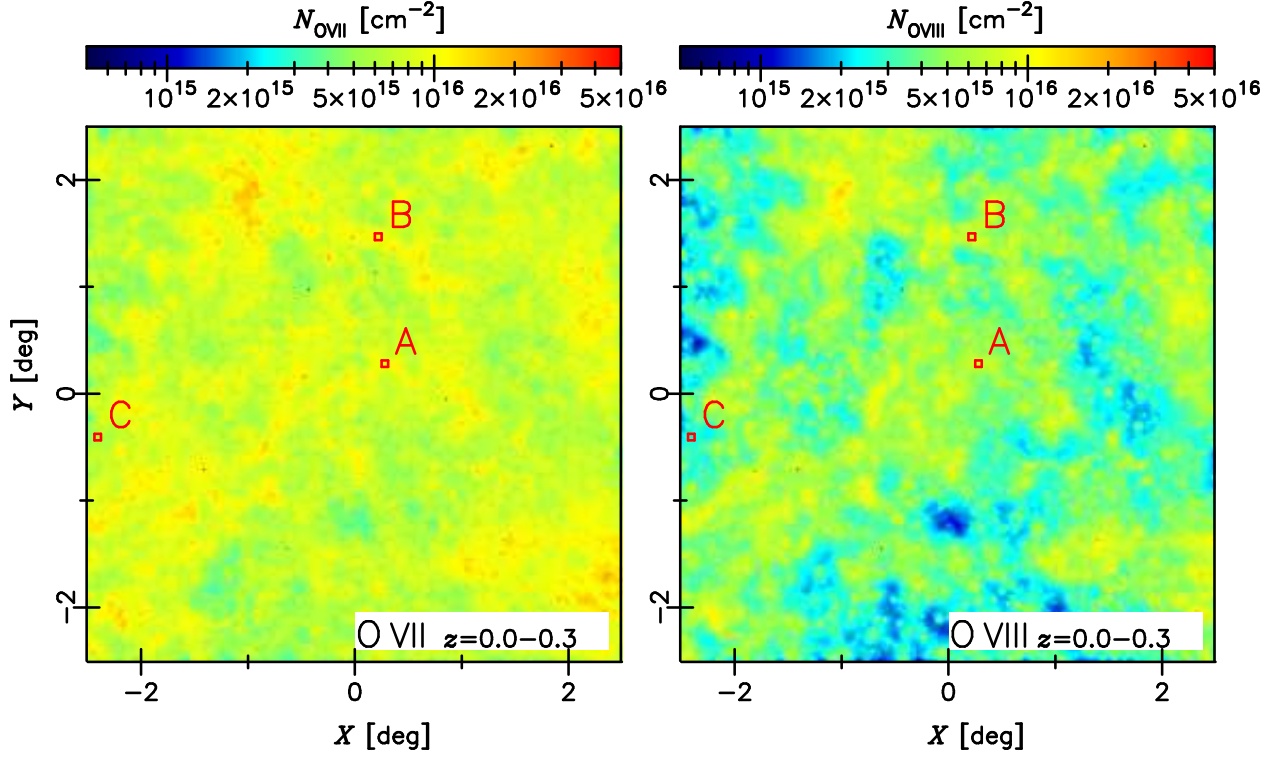


Fig. 7. Column density maps of O VII (*Left*) and O VIII (*Right*) for $0.0 < z < 0.3$. Three red squares labeled A, B, and C indicate the regions corresponding to Figures 8 to 10.

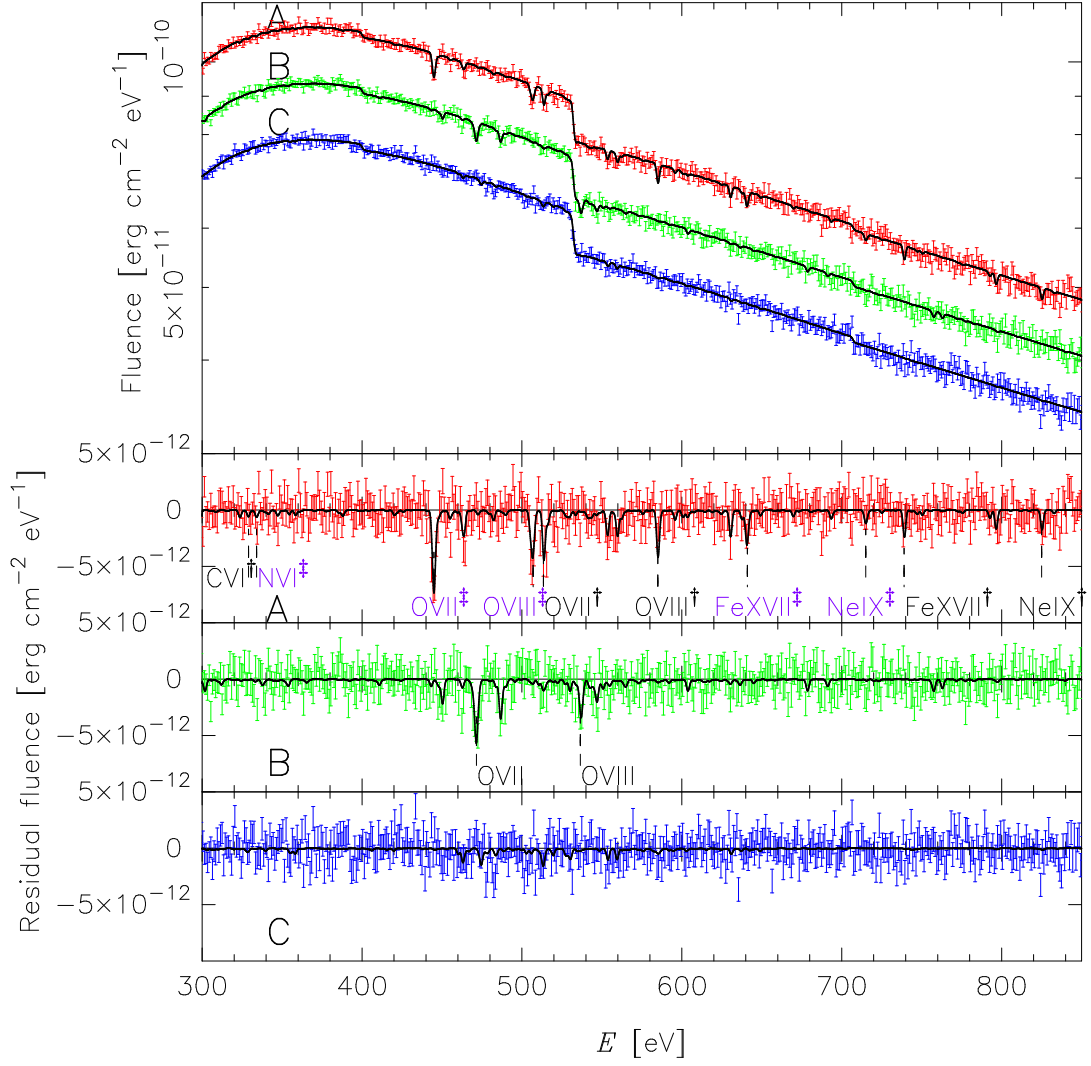


Fig. 8. Mock transmission spectra of a QSO. Top panel plots fluences through three different LOSs (A, B, and C indicated in Figure 7). For an illustrative purpose, curves B and C are artificially multiplied by a factor of $10^{-0.2}$ and $10^{-0.4}$. Lower panels show their residual fluence normalized by the continuum level. The metal line systems with labels \dagger and \ddagger in the spectrum A correspond to the WHIM clumps at $z = 0.12$ (*Upper panels* in Fig.9) and $z = 0.29$ (*Lower panels* in Fig.9), respectively.

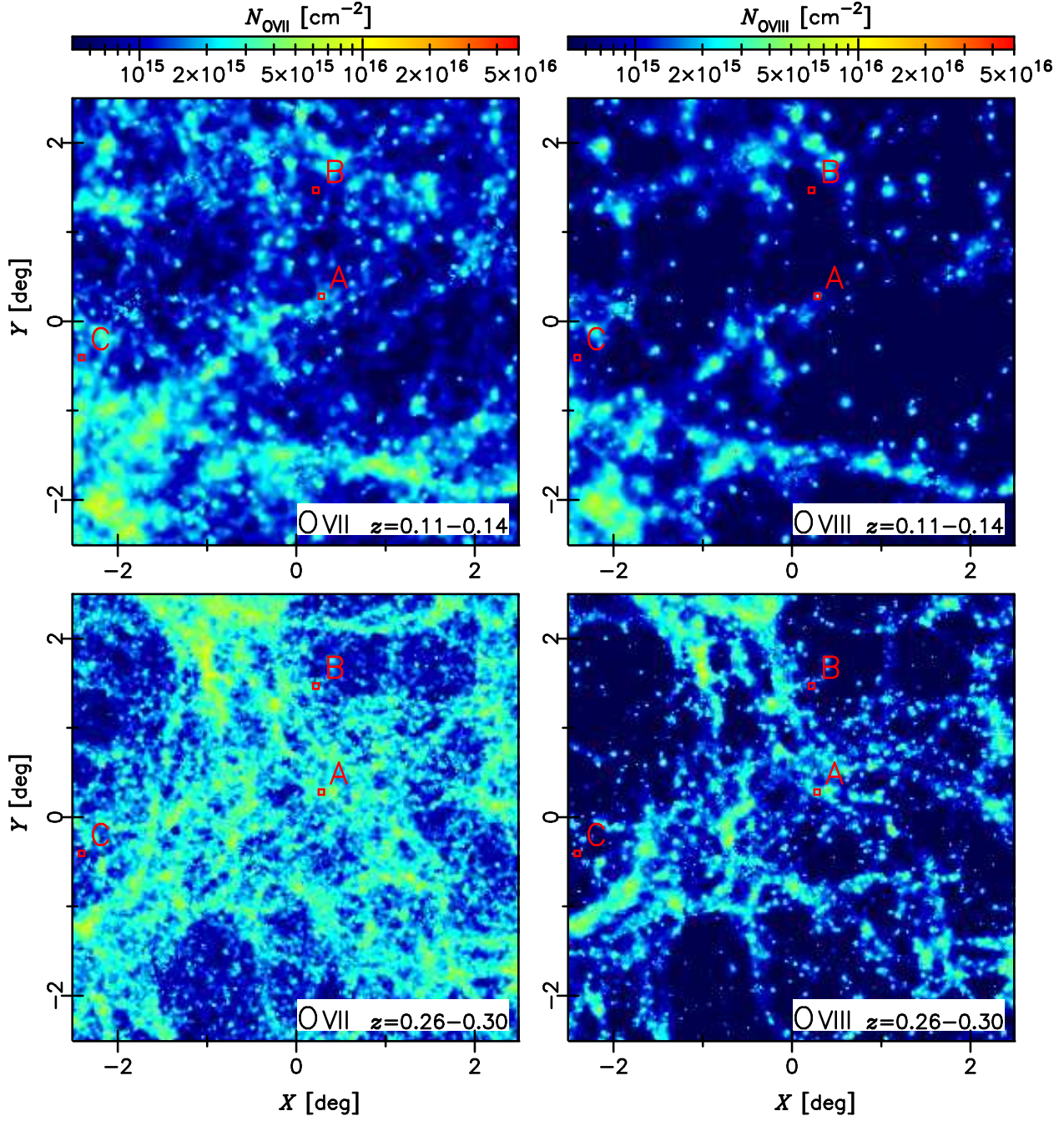


Fig. 9. Column density maps of O VII (*Left*) and O VIII (*Right*) for $0.11 < z < 0.14$ (*Upper*) and for $0.26 < z < 0.30$ (*Lower*).

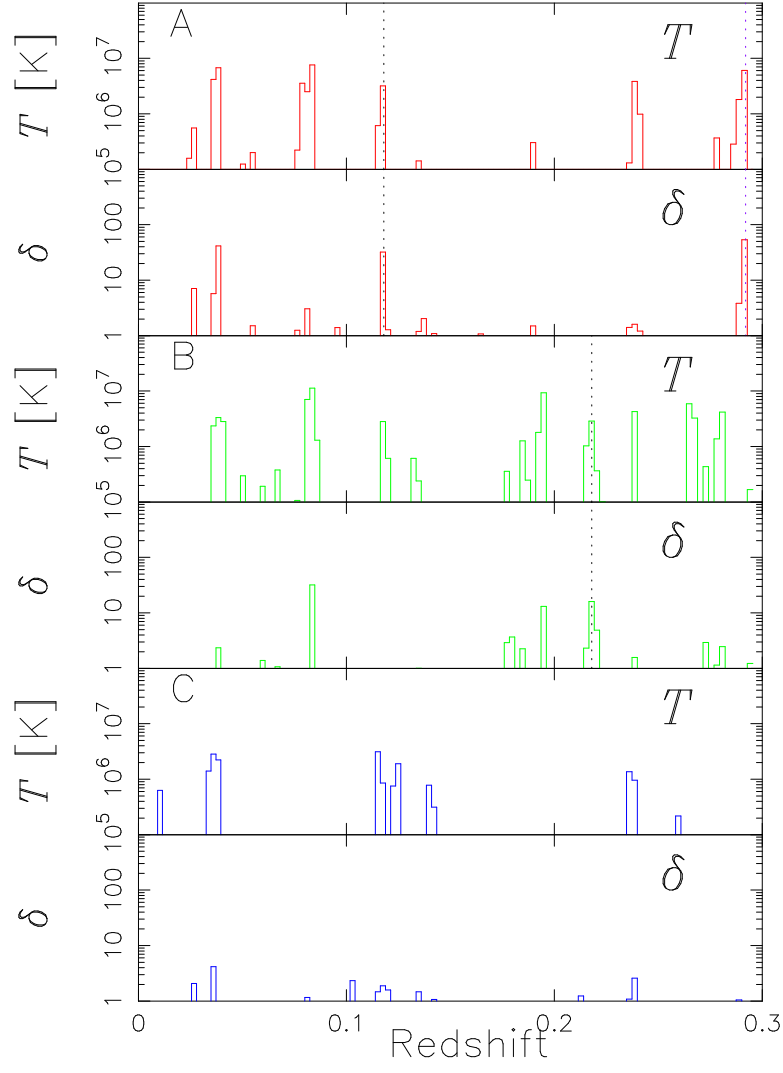


Fig. 10. Redshift distribution of temperature and over-density along the three LOSs A, B, and C (from top to bottom).

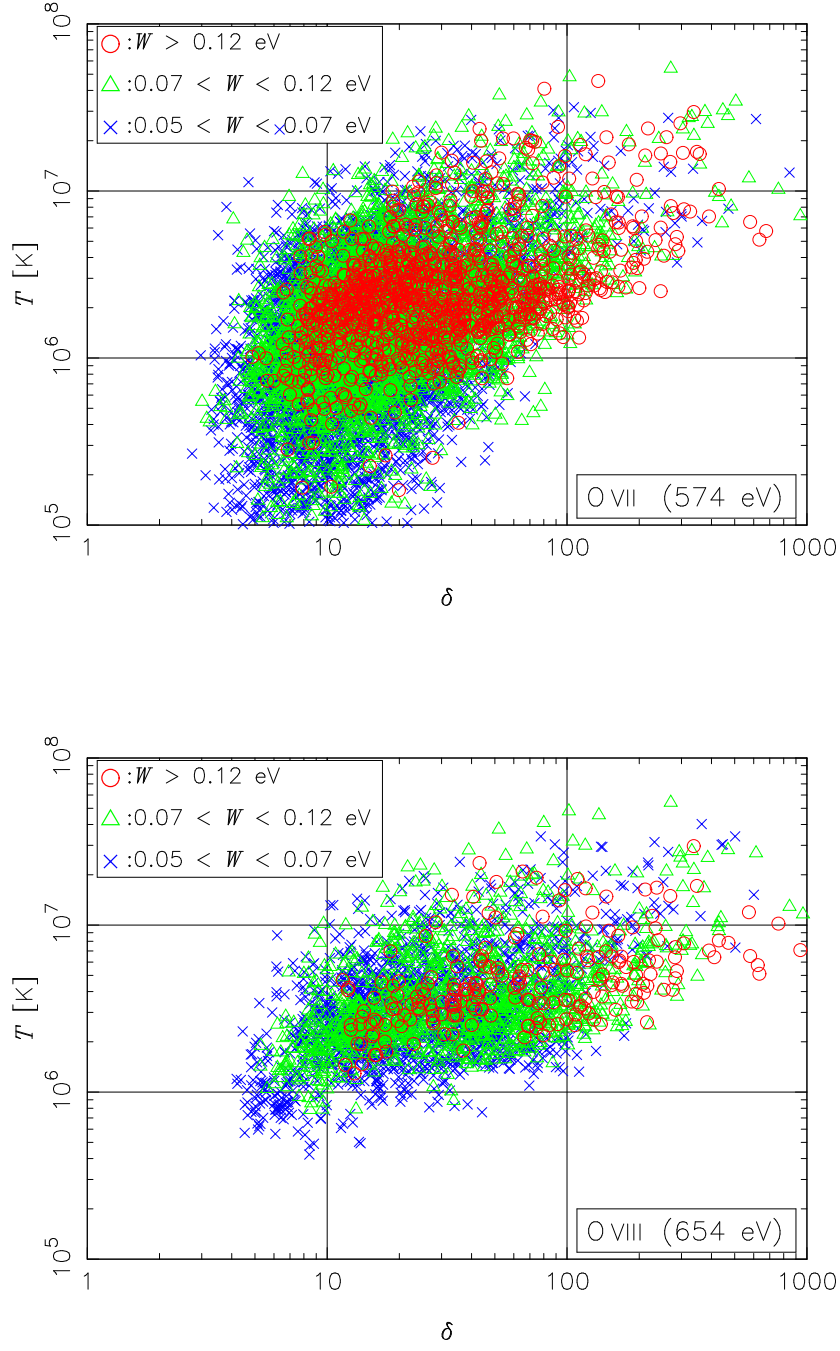


Fig. 11. Scatter plots of over-density and temperature of absorption line systems; O VII 574 eV (*Upper panel*) and O VIII 654 eV (*Lower panel*). Circles, crosses, and triangles correspond to the systems with equivalent width of $W \geq 0.12$ eV, $0.07 \leq W \leq 0.12$ eV, and $0.05 \leq W \leq 0.07$ eV, respectively.

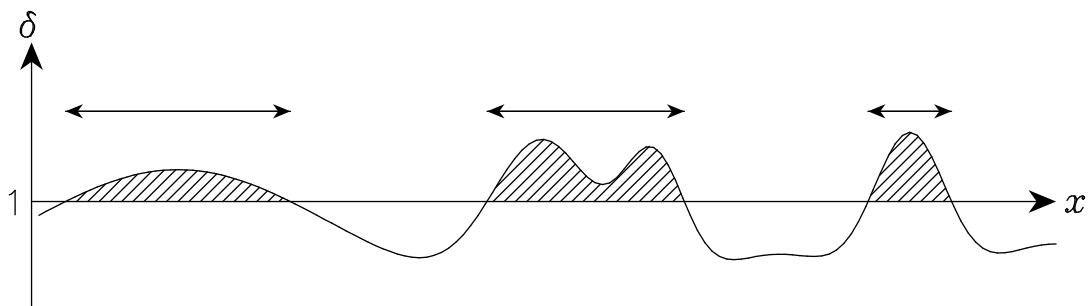


Fig. 12. Schematic identification method of clumps of WHIM.

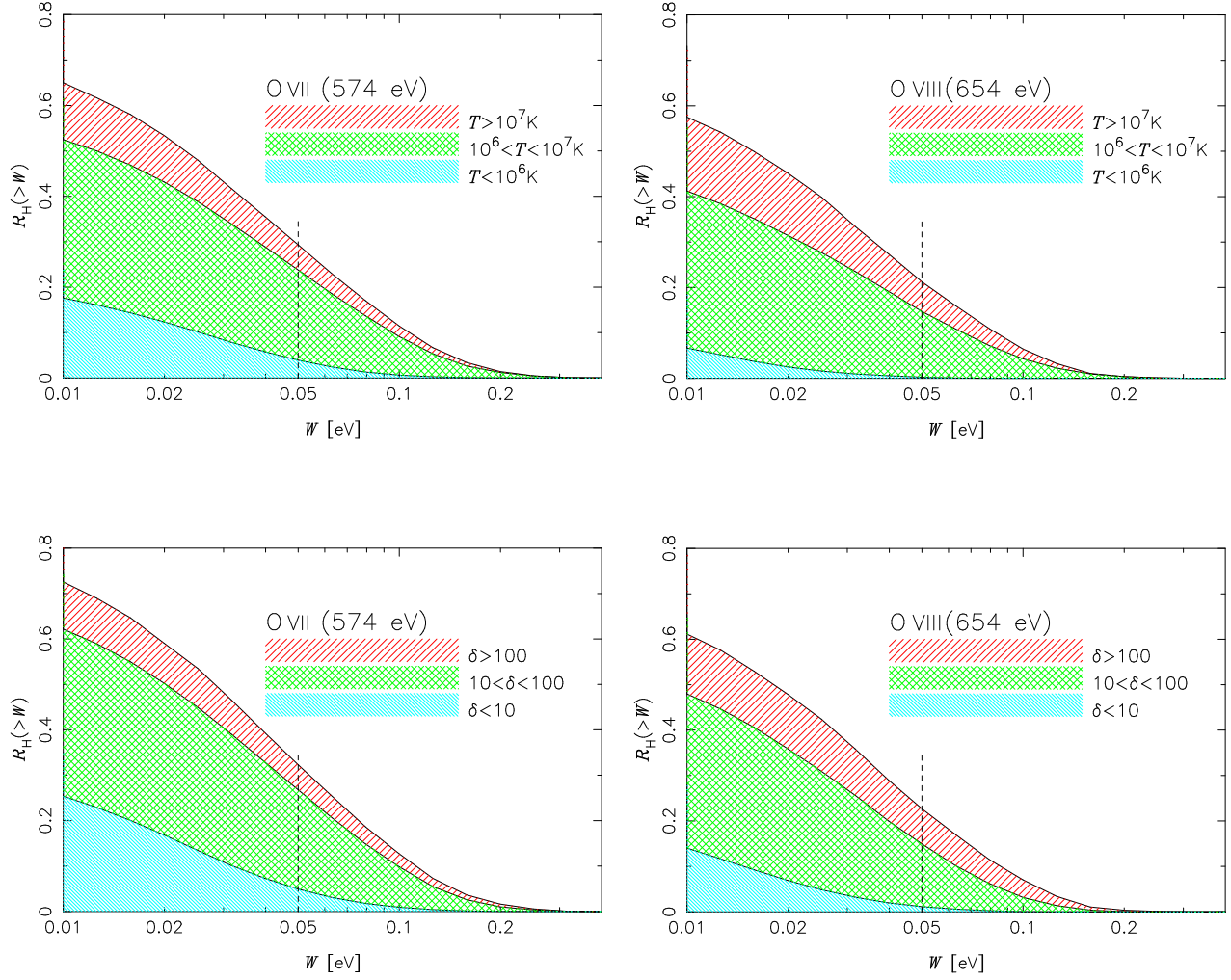


Fig. 13. Cumulative ratio of hydrogen column densities (eq.(26)) as a function of the equivalent width of the detected absorption line systems; OVII 574 eV (*Left*) and O VIII 654 eV (*Right*). The three shaded regions indicate the different temperature (*Upper*) and density (*Lower*) ranges; $T > 10^7$ K, $10^6 < T < 10^7$ K, and $T < 10^5$ K (*Upper*), and $\delta > 100$, $10 < \delta < 100$, and $\delta < 10$ (*Lower*) from top to bottom.

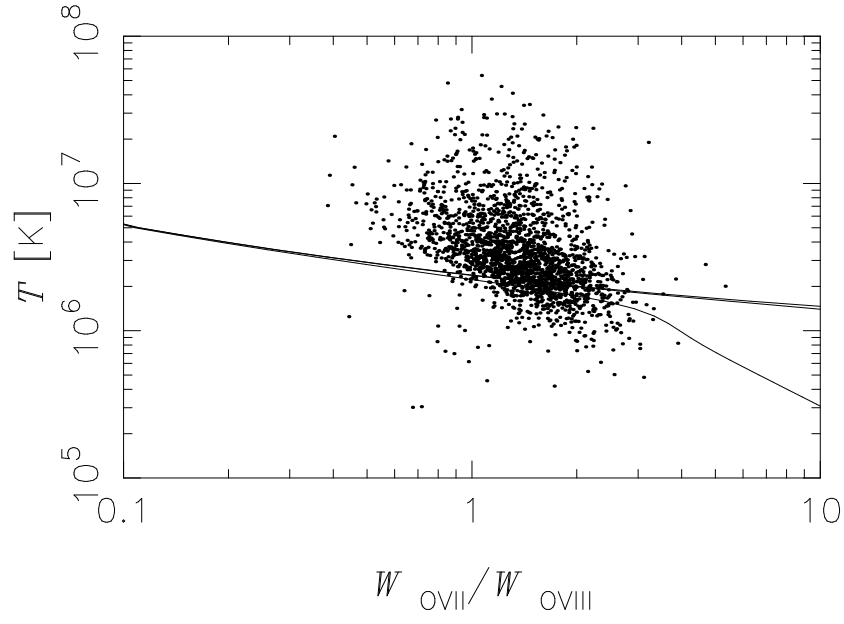


Fig. 14. Ratio of the OVII (574 eV) and O VIII (654 eV) equivalent widths plotted against the mass-weighted average temperature. The solid curves show the theoretical curves in the uniform case under CPlE assuming the hydrogen number density $n_H = 10^{-5}, 10^{-6}$, and 10^{-7} cm^{-3} from top to bottom.

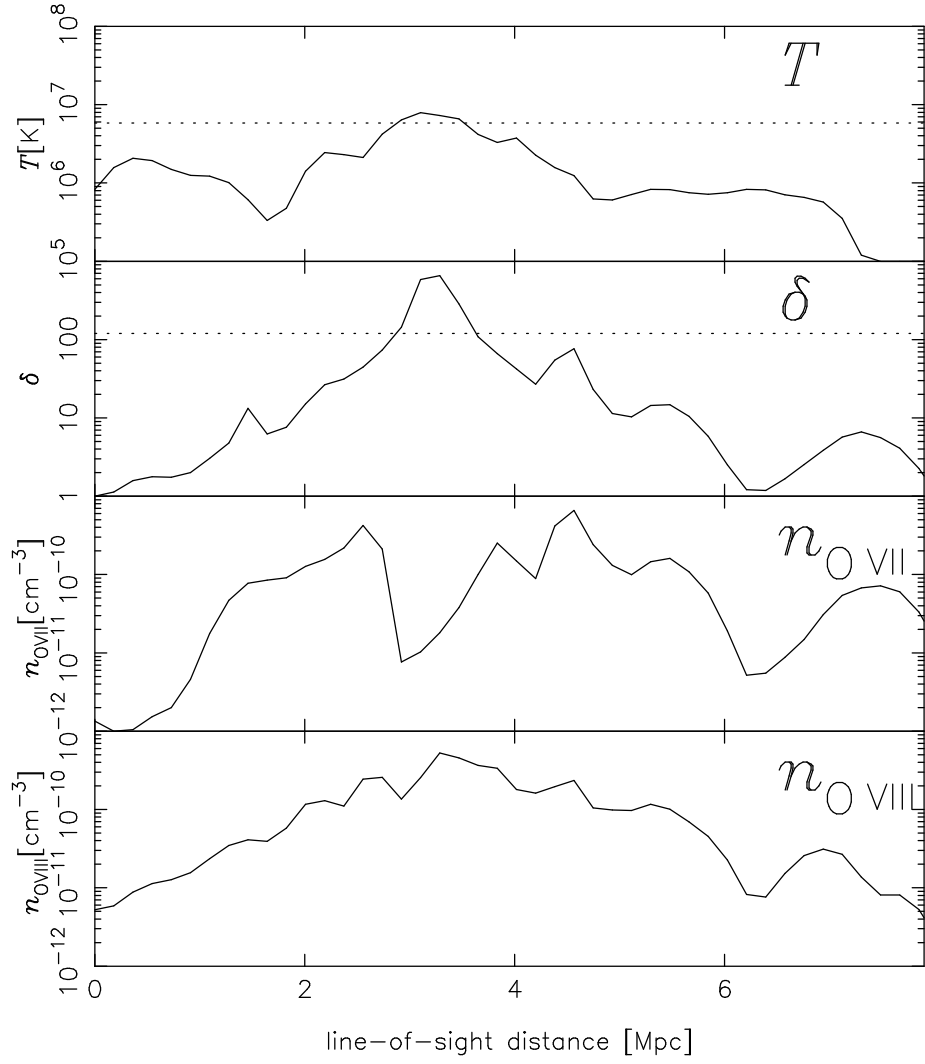


Fig. 15. An example of sub-structure in a WHIM which forms a single absorption line system according to our identification procedure. From top to bottom plotted are temperature, over-density, number density of O VII, and number density of O VIII.

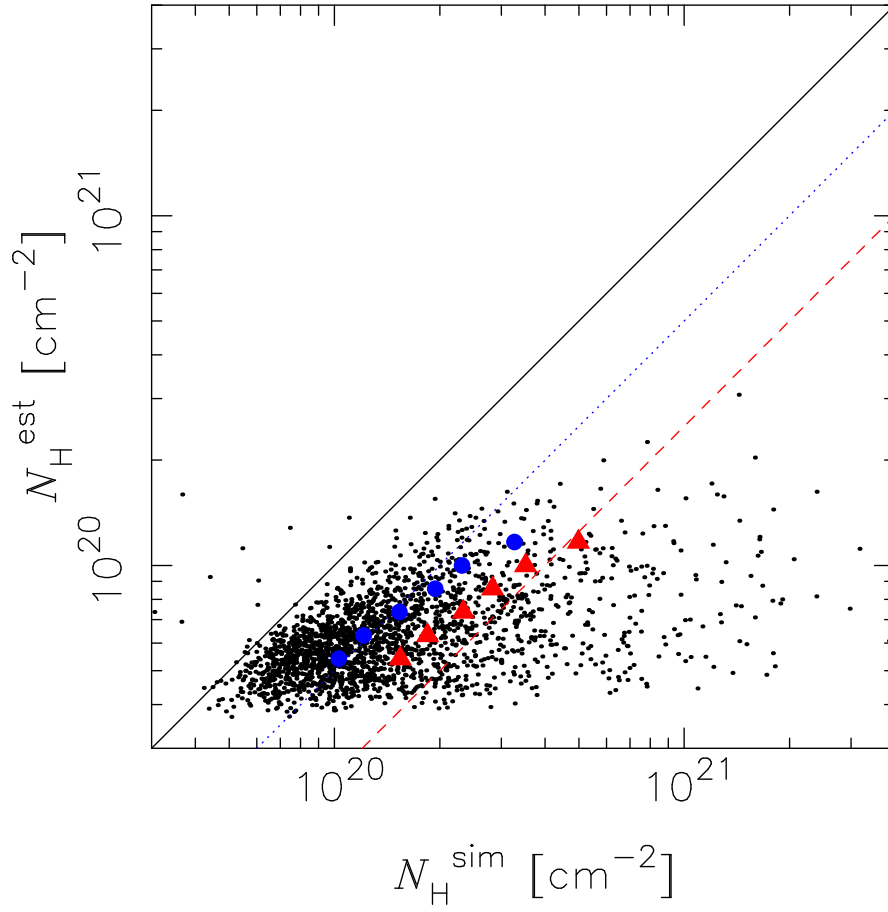


Fig. 16. Comparison between $N_{\text{H}}^{\text{est}}(> 3\sigma)$ and $N_{\text{H}}^{\text{sim}}(> 3\sigma)$. Each dot represents a single WHIM clump which exhibits both OVII and OVIII with $S/N > 3$ (1903 clumps in total). The filled circles and triangles indicate the mean and median values of $N_{\text{H}}^{\text{sim}}(> 3\sigma)$ for the fixed bin with respect to $N_{\text{H}}^{\text{est}}(> 3\sigma)$. The solid, dotted, and dashed lines show $N_{\text{H}}^{\text{est}}(> 3\sigma)/N_{\text{H}}^{\text{sim}}(> 3\sigma) = 1, 1/2$, and $1/4$, respectively.

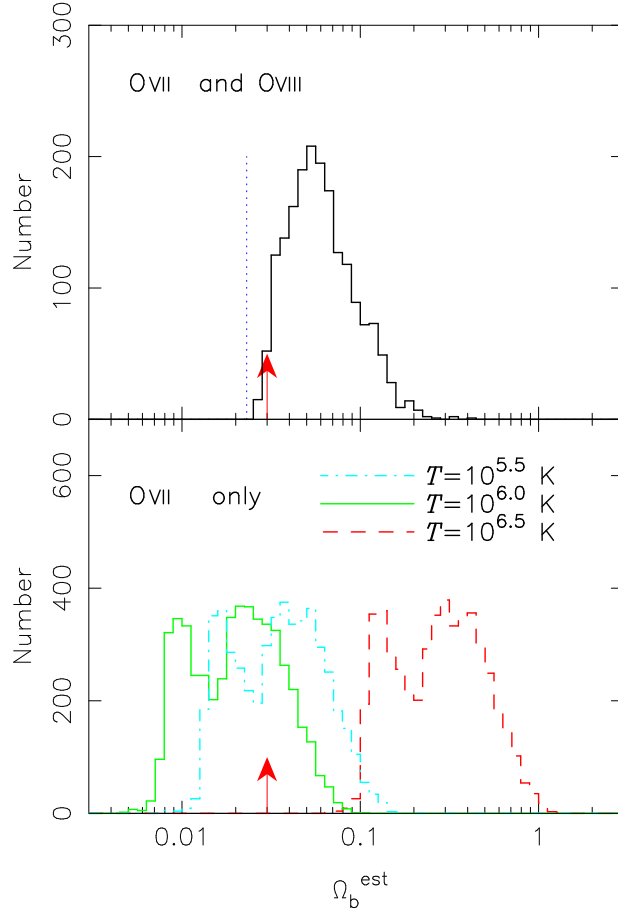


Fig. 17. Histogram of Ω_b^{est} estimated according to eq.(30). The upper panel shows the case that both OVII and OVIII are detected and temperature is estimated from their line ratio. The vertical dotted line is the mean value 0.023 computed from the entire LOSs including non-detection. The lower panel shows an estimation using only O VII absorption lines assuming temperature $T = 10^{5.5}$, $10^{6.0}$, and $10^{6.5}$ K. The arrow indicates the value of $\Omega_b (= 0.03)$ that is adopted in our numerical simulation.